Atmos. Chem. Phys., 16, 15199–15218, 2016
www.atmos-chem-phys.net/16/15199/2016/
doi:10.5194/acp-16-15199-2016


Atmospheric Chemistry and Physics Open Access EGU

# What are the greenhouse gas observing system requirements for reducing fundamental biogeochemical process uncertainty? Amazon wetland $CH_4$ emissions as a case study

**A. Anthony Bloom[1], Thomas Lauvaux[1,2], John Worden[1], Vineet Yadav[1], Riley Duren[1], Stanley P. Sander[1], and David S. Schimel[1]**

[1]Jet Propulsion Laboratory, California Institute of Technology, Pasadena, CA, USA
[2]Department of Meteorology, The Pennsylvania State University, University Park, PA, USA

*Correspondence to:* A. Anthony Bloom (abloom@jpl.nasa.gov)

Received: 13 April 2016 – Published in Atmos. Chem. Phys. Discuss.: 27 April 2016
Revised: 2 November 2016 – Accepted: 8 November 2016 – Published: 8 December 2016

**Abstract.** Understanding the processes controlling terrestrial carbon fluxes is one of the grand challenges of climate science. Carbon cycle process controls are readily studied at local scales, but integrating local knowledge across extremely heterogeneous biota, landforms and climate space has proven to be extraordinarily challenging. Consequently, top-down or integral flux constraints at process-relevant scales are essential to reducing process uncertainty. Future satellite-based estimates of greenhouse gas fluxes – such as $CO_2$ and $CH_4$ – could potentially provide the constraints needed to resolve biogeochemical process controls at the required scales. Our analysis is focused on Amazon wetland $CH_4$ emissions, which amount to a scientifically crucial and methodologically challenging case study. We quantitatively derive the observing system (OS) requirements for testing wetland $CH_4$ emission hypotheses at a process-relevant scale. To distinguish between hypothesized hydrological and carbon controls on Amazon wetland $CH_4$ production, a satellite mission will need to resolve monthly $CH_4$ fluxes at a $\sim 333$ km resolution and with a $\leq 10$ mg $CH_4$ $m^{-2}$ $day^{-1}$ flux precision. We simulate a range of low-earth orbit (LEO) and geostationary orbit (GEO) $CH_4$ OS configurations to evaluate the ability of these approaches to meet the $CH_4$ flux requirements. Conventional LEO and GEO missions resolve monthly $\sim 333$ km Amazon wetland fluxes at a 17.0 and 2.7 mg $CH_4$ $m^{-2}$ $day^{-1}$ median uncertainty level. Improving LEO $CH_4$ measurement precision by $\sqrt{2}$ would only reduce the median $CH_4$ flux uncertainty to 11.9 mg $CH_4$ $m^{-2}$ $day^{-1}$. A GEO mission with targeted observing capability could resolve fluxes at a 2.0–2.4 mg $CH_4$ $m^{-2}$ $day^{-1}$ median precision by increasing the observation density in high cloud-cover regions at the expense of other parts of the domain. We find that residual $CH_4$ concentration biases can potentially reduce the $\sim 5$-fold flux $CH_4$ precision advantage of a GEO mission to a $\sim 2$-fold advantage (relative to a LEO mission). For residual $CH_4$ bias correlation lengths of 100 km, the GEO can nonetheless meet the $\leq 10$ mg $CH_4$ $m^{-2}$ $day^{-1}$ requirements for systematic biases $\leq 10$ ppb. Our study demonstrates that process-driven greenhouse gas OS simulations can enhance conventional uncertainty reduction assessments by quantifying the OS characteristics required for testing biogeochemical process hypotheses.

## 1 Introduction

Quantitative knowledge of biogeochemical processes regulating global carbon–climate feedbacks remains highly uncertain (Friedlingstein et al., 2013). Quantifying the sensitivity of biogeochemistry to climate variables directly from observations of atmospheric concentrations has long been a goal of researchers (Bacastow et al., 1980; Vukicevic et al., 2001; Gurney et al., 2008). Estimating the climate sensitivity of carbon fluxes is complicated by both the spatial scale and structure of climate anomalies and the variations of factors affecting ecosystem responses: soils, vegetation, land use and natural disturbance (King et al., 2015). Current ground-based and even space-based carbon cycle observing

systems (OSs) produce flux estimates at continental or even zonal resolution, limiting direct estimation of relationships between climate forcing, ecosystem properties and carbon fluxes (Huntzinger et al., 2012; Peylin et al., 2013). The uncertainty of carbon fluxes at continental and finer scales is high, and different systems for flux estimation often produce strikingly different spatial patterns (Schimel et al., 2015a; Bloom et al., 2016). Because of the high uncertainty in the spatial regionalization of fluxes, some of the most compelling studies of carbon and climate have eliminated the spatial information and instead have used correlative approaches to identify the regions likely to be responsible for observed global concentration anomalies (Braswell et al., 1997; Cox et al., 2013; Chen et al., 2015; Franklin et al., 2016).

The expansion of surface and aircraft observing networks has increased our understanding of the carbon cycle and is essential for precise quantification of trace-gas concentrations (Andrews et al., 2014; Sweeney et al., 2015; Wilson et al., 2016). Surface networks are intrinsically limited in their density, by cost, access to remote terrestrial and marine environments, environmental conditions and other logistical constraints (Schimel et al., 2015b). The first-generation trace-gas observing satellites were designed to make global-scale measurements of concentrations with unprecedented frequency and accuracy but were not designed to test specific hypotheses about biogeochemical processes. The successes of GOSAT (Yokota et al., 2009) and OCO-2 (Crisp et al., 2004) open the door to designing a next generation of spaceborne greenhouse gas measurements to test specific hypotheses about the terrestrial biosphere or the oceans. In this paper, we report an observing system design exercise aimed at identifying the observing system needed to increase understanding of a long-standing uncertainty in the global carbon budget, specifically the role of tropical wetlands in the global $CH_4$ budget (Mitsch et al., 2010; Bloom et al., 2010; Melton et al., 2013). While we focus this analysis on $CH_4$, we note that the models and methodology are equally applicable to other gases (such as $CO_2$), as well as other regions or mechanisms.

### 1.1 Wetland $CH_4$ emissions

Biogenic methane ($CH_4$) emission processes are one of the principal components of global carbon–climate interactions; $CH_4$ is a potent greenhouse gas (Myhre et al., 2013) and wetlands account for roughly 20–40 % of the global $CH_4$ source (Kirschke et al., 2013). The processes controlling the magnitude and temporal evolution of $CH_4$ outgassing from wetland environments remain largely unquantified on continental scales. As a result, global-scale wetland $CH_4$ emissions (Melton et al., 2013) and their role in the interannual growth of atmospheric $CH_4$ remain highly uncertain.

Global wetland $CH_4$ emissions largely depend on soil inundation, temperature and substrate carbon availability. The major sources of wetland $CH_4$ emissions include boreal North America, boreal Eurasia, the Indonesian archipelago, the Congo and Amazon River basins (Fig. 1, map), which are all characterized by high soil carbon content (Hiederer and Köchy, 2011) and substantial seasonal or year-round inundation extent (Prigent et al., 2012). By and large, Amazon wetland $CH_4$ emissions dominate both the magnitude and uncertainty of global wetland $CH_4$ emissions (Melton et al., 2013). Estimates of Amazon wetland $CH_4$ emissions range between 20 and 60 Tg $CH_4$ year$^{-1}$ (Fung et al., 1991; Riley et al., 2011; Bloom et al., 2012; Melack et al., 2004), roughly equivalent to 10–30 % of the global wetland $CH_4$ source. Major uncertainties are also associated with the spatial and temporal variability of $CH_4$ emissions (Fig. 1). Uncertainties in tropical wetland $CH_4$ emission estimates largely stem from a lack of quantitative knowledge of process controls on wetland $CH_4$ emissions and a lack of data constraints on the drivers of wetland emissions. In terms of processes, a range of factors including soil pH, wetland vegetation cover, wetland depth, salinity and air–water gas exchange dynamics, likely impose fundamental controls on the rate of wetland $CH_4$ emissions. On a continental scale, spatially explicit knowledge of carbon cycling and inundation remain highly uncertain in the wet tropics, primarily due to a sparse in situ measurement network, high cloud cover and biomass density.

### 1.2 Top-down $CH_4$ flux estimates

Top-down constraints on $CH_4$ fluxes – from atmospheric $CH_4$ observations – are key to retrieving quantitative information on continental-scale $CH_4$ biogeochemistry (Bousquet et al., 2011; Pison et al., 2013; Basso et al., 2016; Wilson et al., 2016). Low-earth orbit (LEO) satellite missions, including SCIAMACHY, IASI, TES and GOSAT, have surveyed global $CH_4$ concentrations for over a decade (Frankenberg et al., 2008; Crevoisier et al., 2009; Butz et al., 2011; Worden et al., 2012). In particular, column $CH_4$ retrievals from SCIAMACHY have proven sensitive to wetland and other $CH_4$ emissions (Bloom et al., 2010; Bergamaschi et al., 2013). However, cloud cover is a major inhibiting factor when measuring atmospheric greenhouse gas concentrations within the proximity of tropical wetland regions. In particular, densely vegetated seasonally inundated areas of the Amazon and Congo River basins can experience more than 95 % monthly mean cloud cover. With fewer cloud-free observations of lower tropospheric $CH_4$ concentrations, atmospheric inversion estimates of wetland $CH_4$ emissions remain exceedingly difficult, especially in the absence of well-characterized prior information on the magnitude, location and timing of emissions.

Atmospheric inverse estimates of $CH_4$ emissions are expected to improve with tropospheric $CH_4$ measurements from the upcoming ESA TROPOMI mission (Butz et al., 2012; Veefkind et al., 2012). Furthermore, geostationary missions (such as GEOCAPE) will potentially provide the measurements needed to substantially improve $CH_4$ emission es-

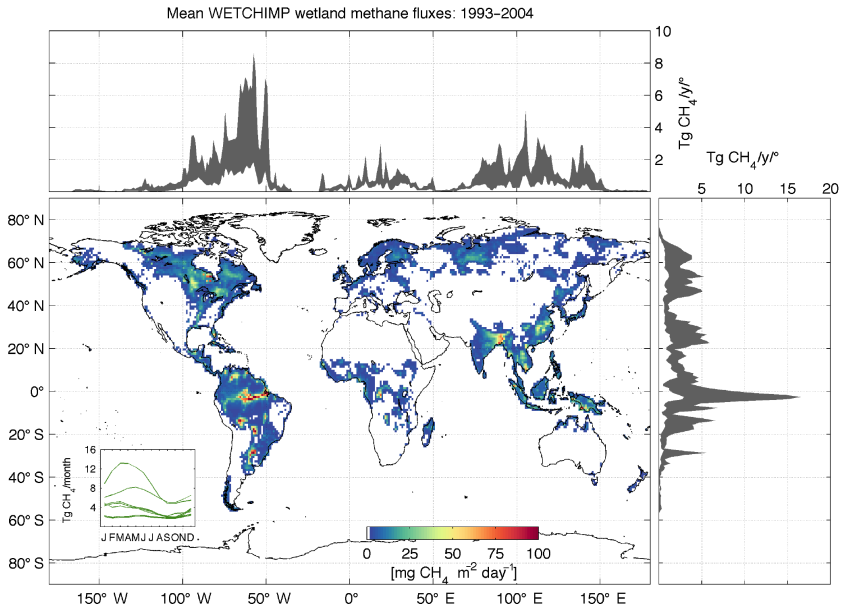


**Figure 1.** Mean annual wetland and rice $CH_4$ emissions (central map), and associated longitudinal and latitudinal uncertainty (grey bands), based on the WETCHIMP model inter-comparison project (Melton et al., 2013). Inset: WETCHIMP model total Amazon basin monthly $CH_4$ emissions.

timates (Wecht et al., 2014; Bousserez et al., 2016). Ultimately, the precision and sampling configuration of atmospheric $CH_4$ observations both determine the OS capability of retrieving surface $CH_4$ fluxes. It is currently unclear whether future $CH_4$ measurements will be sufficient to resolve key $CH_4$ fluxes – such as the Amazon basin wetlands – at a process-relevant resolution.

In this study we characterize the satellite observations required to quantify the biogeochemical process controls on Amazon wetland $CH_4$ emissions. Specifically, we identify and characterize the Amazon $CH_4$ emission processes (Sect. 2.1), define the process-relevant $CH_4$ flux resolution and precision required to statistically distinguish between hypothesized wetland $CH_4$ emission scenarios based on several hydrological and carbon datasets (Sect. 2.2), simulate atmospheric measurements throughout the Amazon basin for a range of LEO and geostationary orbit (GEO) satellite OSs, and derive the corresponding $CH_4$ flux uncertainty using an idealized atmospheric inversion (Sect. 2.3). Based on our results, we establish the OS requirements and discuss the potential of future OSs to resolve Amazon wetland $CH_4$ emission processes (Sect. 3). We conclude our paper in Sect. 4.

## 2 Methods

We construct an Observing System Simulation Experiment (OSSE) dedicated to characterizing the spaceborne OS needed to resolve the processes controlling wetland $CH_4$ fluxes from Amazon basin (Fig. 2). Our OSSE involves the following three steps: we (1) characterize the variability of wetland $CH_4$ process controls, (2) define $CH_4$ flux resolution and precision requirements and (3) derive the atmospheric $CH_4$ concentration OS requirements. We define the atmospheric $CH_4$ OS requirement as the ability to meet the $CH_4$ flux resolution and precision requirements during the cloudiest time of year. We focus our analysis on March 2007: all temporally resolved carbon and hydrological observations chosen for this study overlap in 2007, and March 2007 mean cloud cover (84 %) amounts to the highest cloud cover across the whole Amazon River basin within the January–April 2007 wet season (cloud-cover range = 76–84 %) and is considerably higher than the June–September 2007 dry season cloud cover (46–56 %).

### 2.1 Wetland process controls

Wetland $CH_4$ emissions are controlled by a range of biogeochemical processes: inundation is likely to be a first-order control of wetland emissions, as soil $CH_4$ production largely occurs in oxygen-depleted soils (Whalen, 2005). However, extensive studies of wetland $CH_4$ emissions suggest that inundation is not the sole determinant of spatial and temporal $CH_4$ emission dynamics. $CH_4$ can be transferred directly into the atmosphere via macrophytes, thus circumventing the aerobic soil layer (Whalen, 2005). Water-body depth (Mitsch et al., 2010), type (Devol et al., 1990) and aquatic macrophyte density (Laanbroek, 2010) can affect the proportion of wetland $CH_4$transferred to the atmosphere.

Carbon (C) availability is also a determinant of wetland $CH_4$ emissions. Methanogen-available C turnover rates

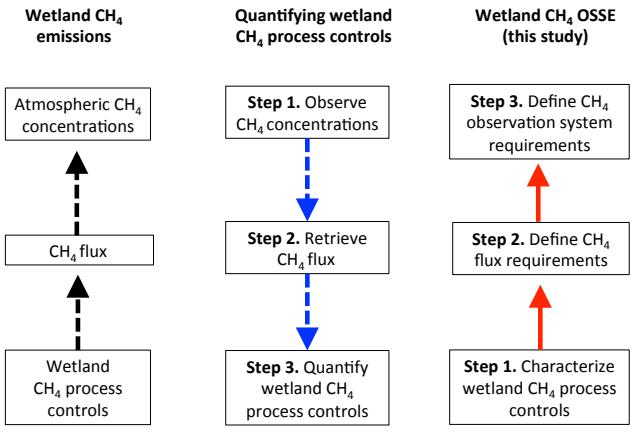


**Figure 2.** Wetland $CH_4$ emissions into the atmosphere are regulated by wetland biogeochemical processes (left column). Continental-scale wetland $CH_4$ process controls can be retrieved by (i) resolving surface $CH_4$ fluxes from retrieved satellite $CH_4$ observations and (ii) resolving process parameters from retrieved $CH_4$ fluxes (middle column). The optimal satellite $CH_4$ observation requirements are a function of the flux resolution and precision required to resolve wetland $CH_4$ process controls (right column): OSSE steps 1–3 are described in Sects. 2.1–2.3.

(Miyajima et al., 1997), composition (Wania et al., 2010), temporal dynamics (Bloom et al., 2012) and C stocks together drive spatial and temporal variability of carbon limitation on $CH_4$ production in wetlands. C cycle state variables, including the spatial variability of total biomass (Saatchi et al., 2011; Baccini et al., 2012) and soil carbon (Hiederer and Köchy, 2011), vary at $< 1000$ km scales. Methanogen-available C sources – such as gross primary production (GPP) and leaf litter – vary substantially at monthly timescales in the wet tropics (Beer et al., 2010; Chave et al., 2010; Caldararu et al., 2012). In the next section, we establish the $CH_4$ flux resolution and precision requirements based on the variability of potential tropical wetland $CH_4$ emissions process controls (namely carbon uptake, live biomass and dead organic matter stocks, inundation and precipitation).

## 2.2 Wetland $CH_4$ flux requirements

Here we define a set of wetland $CH_4$ flux precision and resolution requirements suitable for the formulation and testing of wetland $CH_4$ emissions process control hypotheses. Measurement and model-based analyses of Amazon wetland $CH_4$ emissions provide a range of contradictory estimates on spatial patterns and seasonality (Devol et al., 1990; Riley et al., 2011; Bloom et al., 2012; Melton et al., 2013; Basso et al., 2016) suggesting that the basin-wide process controls on wetland $CH_4$ emissions remain virtually unknown. Here, our aim is to provide a first-order, model-independent characterization of wetland $CH_4$ flux resolution and precision requirements based on the basin-wide variations in carbon and hydrological processes. Our resolution requirement is based on the correlation lengths of hypothesized wetland $CH_4$ emission process controls. At the required resolution, our precision requirement is that wetland $CH_4$ emissions scenarios – derived from a range of hypothesized carbon and hydrological process controls – are (a) statistically inter-distinguishable and (b) distinguishable from a spatiotemporally uniform wetland $CH_4$ flux (i.e., a null hypothesis).

Given our process-level understanding of wetland $CH_4$ emissions, we propose four carbon and three hydrological proxies as the dominant drivers of wetland $CH_4$ emission variability (C1–C4 and H1–H3 respectively). We use carbon stocks and fluxes as proxies for variation in C availability for wetland $CH_4$ production. We characterize the spatial variability of carbon uptake based on the Jung et al. (2009) eddy-covariance-based monthly $0.5° \times 0.5°$ GPP product (C1) and monthly $0.5° \times 0.5°$ solar-induced fluorescence retrieved from the Global Ozone Monitoring Experiment measurements (Joiner et al., 2013; C2). We use the Saatchi et al. (2011) biomass map (C3) and the Harmonized World Soil Database soil carbon stocks (C4; Hiederer and Köchy, 2011). We define the spatial variability of hydrological controls over methane flux based on two inundation fraction datasets (Prigent et al., 2012; Schroeder et al., 2015; H1 and H2) and the NASA Tropical Rainfall Measuring Mission (TRMM; Huffman et al., 2007) precipitation retrievals (H3).

### 2.2.1 $CH_4$ flux resolution

Our resolution requirement is based on a first-order assessment of the process variable correlation length scales: we anticipate that retrieving wetland $CH_4$ fluxes at much finer scales may be redundant, while retrieving fluxes at much coarser scales may hinder the potential to investigate biogeochemical process controls on wetland $CH_4$ emission variability. We use an autocorrelative approach to identify the variability length scales of potential $CH_4$ emissions process controls (see Appendix A). The spatial autocorrelation coefficients (Moran's I) of the seven limiting process variables indicate coherent spatial structures spanning up to $\sim$ 333–666 km across the Amazon River basin (Fig. 3): process variables exhibit high autocorrelation at a $1° \times 1°$ resolution ($L \sim 111$ km) and no significant spatial correlation at $6° \times 6°$ ($L \sim 666$ km). Based on our correlative analysis, we expect that wetland $CH_4$ flux estimates at $3° \times 3°$ ($L \sim 333$ km) will likely be critical for a first-order distinction between the roles of carbon and water processes on Amazon wetland $CH_4$ emissions: we propose a $\sim 333$ km $CH_4$ flux resolution as the spatial resolution required to determine the role of process control variability on wetland $CH_4$ emissions. For all time-varying datasets (C1, C4, H1, H2 and H3), we conducted a lagged Pearson's correlation analysis: the time-varying datasets indicate varying levels of statistically significant 1-month autocorrelations across the study region (percent of area exhibiting significant auto-

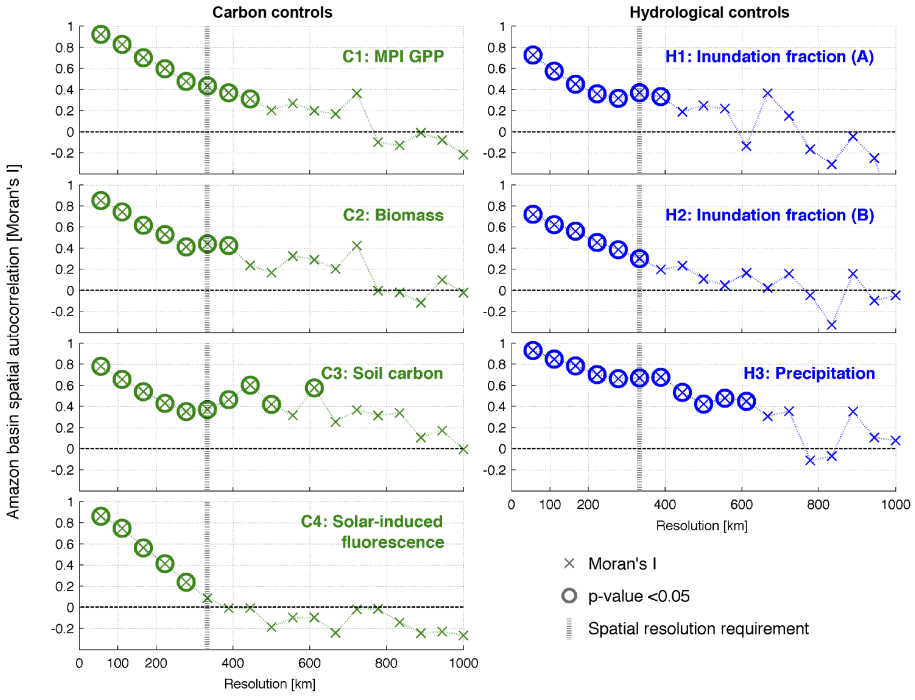


**Figure 3.** Spatial autocorrelation (Moran's I) for potential carbon controls (left column) and hydrological controls (right column) on wetland $CH_4$ emissions. The spatial variability of carbon controls are derived from satellite observations (biomass in Saatchi et al., 2011; solar-induced fluorescence in Joiner et al., 2013), the Harmonized World Soil Database (soil carbon; Hiederer and Köchy, 2011) and FLUXNET-derived GPP (Jung et al., 2009). The spatial variability estimates for hydrological controls are based on satellite measurements of inundation (A: Prigent et al., 2012; B: Schroeder et al., 2015) and precipitation (the NASA Tropical Rainfall Measuring Mission). Significant Moran's I values (where the Moran's I $p$ value $< 0.05$) are highlighted as circles. We set a $\sim 333$ km spatial resolution requirement for monthly $CH_4$ flux retrievals, based on the maximum correlation lengths of potential carbon and hydrological controls on wetland $CH_4$ emissions. The details of the Moran's I analysis are fully described in Appendix A.

correlations: C1 = 98 %; C4 = 6 %; H1 = 47 %; H2 = 51 %; H3 = 64 %), while virtually 0 % of the study region exhibits significant 2-month temporal autocorrelations. For this study, we opt for a monthly temporal resolution requirement; however, we note that higher-temporal-resolution datasets (given their availability) can potentially provide an improved assessment of the temporal correlation scales of carbon and hydrological process controls.

### 2.2.2 $CH_4$ flux precision

We next derive the $CH_4$ flux precision required to distinguish between hypothesized wetland $CH_4$ process controls at a $\sim 333$ km monthly resolution. We derive the precision requirements assuming 1 continuous year of $CH_4$ flux retrievals. We formulate (a) spatial $CH_4$ emission hypotheses, where wetland $CH_4$ emissions linearly co-vary with the hypothesized processes at $\sim 333$ km scales, and (b) temporal $CH_4$ emission hypotheses, where wetland $CH_4$ emissions linearly co-vary with the hypothesized processes on monthly timescales. Our motivation for evaluating both spatial and temporal hypotheses is that we do not necessarily expect the spatial and temporal process controls on wetland $CH_4$ emissions to be the same. For example, Amazon wetland $CH_4$ emissions could be spatially limited by carbon uptake (GPP) and temporally driven by inundation. Each wetland hypothesis is scaled to an annual mean flux of 12 mg $m^{-2}$ $day^{-1}$, which corresponds to the Melack et al. (2004) annual Amazon-wide wetland $CH_4$ emission estimate (29.3 Tg $CH_4$ $year^{-1}$ across 668 Mha). The explicit formulation of spatial and temporal wetland $CH_4$ emission hypotheses is described in Appendix B.

For a range of retrieved $CH_4$ flux precisions across the Amazon basin (spanning 1–100 mg $m^{-2}$ $day^{-1}$), we test whether each spatial and temporal wetland $CH_4$ emission hypothesis is statistically distinct from alternative hypotheses and a "no variability" hypothesis (i.e., a null hypothesis); the derivation of the statistical confidence in distinguishing between hypotheses is described in Appendix B. The distinction confidence (%) for spatial and temporal hypotheses is shown in Fig. 4: at a monthly $\sim 333$ km resolution, both spatial and temporal wetland $CH_4$ emission hypotheses are inter-distinguishable with $> 95$ % confidence at a $\leq 10$ mg $m^{-2}$ $day^{-1}$ $CH_4$ flux precision.

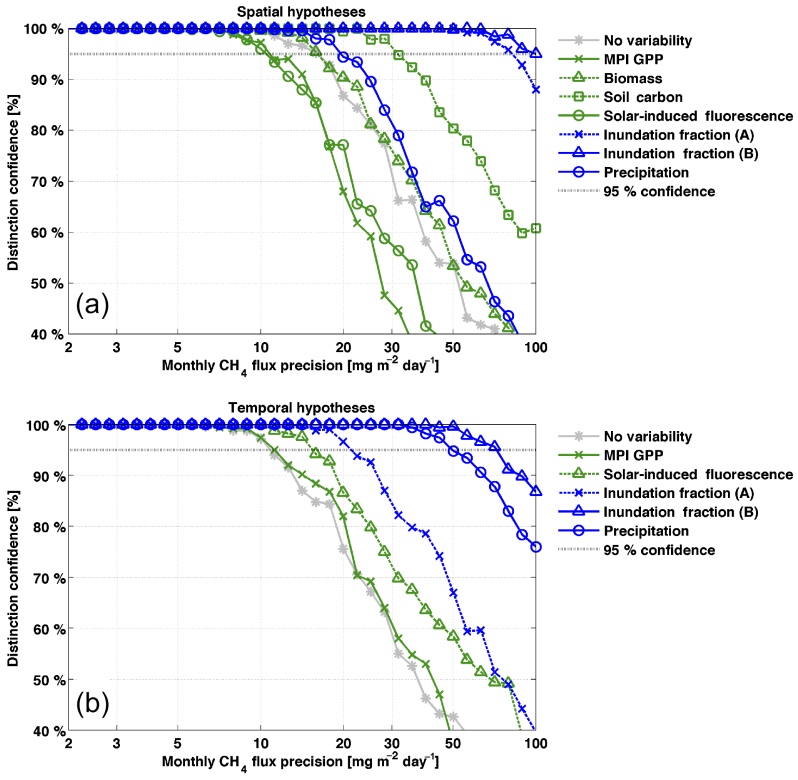


**Figure 4.** Distinction confidence between Amazon basin spatial and temporal wetland $CH_4$ emission hypotheses against monthly $\sim 333$ km $CH_4$ flux precision. Spatial and temporal wetland $CH_4$ emission hypotheses are distinguishable with a 95 % confidence at a $\leq 10\,\mathrm{mg\,m^{-2}\,day^{-1}}$ precision. For this study we define our $\sim 333$ km $CH_4$ flux precision requirement as $10\,\mathrm{mg\,m^{-2}\,day^{-1}}$.

### 2.2.3 $CH_4$ requirements

Given the spatial and temporal variability of potential hydrological and carbon controls, we define the following requirements for wetland $CH_4$ flux retrievals:

- $\sim 333$ km spatial resolution
- monthly temporal resolution
- $10\,\mathrm{mg\,CH_4\,m^{-2}\,day^{-1}}$ precision.

Our resolution and precision requirements provide a first-order assessment of the wetland $CH_4$ emission biogeochemical process control variability. We anticipate that satellite-based $CH_4$ flux estimates meeting the above-stated requirements will provide robust characterization of spatial variation in Amazon wetland $CH_4$ emissions on the scale of variation in the major carbon and water controls, allowing forcing (hydrology and carbon) and response ($CH_4$ flux) to be related directly. Therefore, by retrieving $CH_4$ fluxes at the required resolution and precision, carbon and hydrological process hypotheses on the dominant drivers of Amazon wetland $CH_4$ emissions can be adequately investigated. However, depending on the nature of the scientific investigation, we recognize that the trade-off space between spatial resolution, temporal resolution, precision and study duration can be further explored to derive an optimal combination of $CH_4$ flux requirements.

Throughout the next subsections, we characterize the required satellite column $CH_4$ measurements needed to resolve $CH_4$ flux with the above-stated requirements. To quantify the sensitivity of our results to the above-mentioned requirements, we repeat our analysis for a range of $CH_4$ flux spatial resolution requirements ($L = 150$–$990$ km) and we derive the corresponding $CH_4$ flux precision requirements.

## 2.3 $CH_4$ observation requirements

We define the atmospheric $CH_4$ observation requirements by retrieving $CH_4$ fluxes from a range of LEO and GEO OS simulated $CH_4$ retrieved concentrations, or "observations". Our approach is three-fold: (a) we simulate LEO and GEO $CH_4$ observations for March 2007; (b) we derive the precision of $CH_4$ measurement averaged at an $L \times L$ resolution (henceforth the "cumulative $CH_4$ measurement precision"); and (c) we employ an idealized inversion to simulate $CH_4$ flux retrieval uncertainty for March 2007 based on the cumulative $CH_4$ measurement precision. We note that wetland emissions are the largest and most uncertain source of $CH_4$ within the Amazon River basin (Wilson et al., 2016; Melton et al., 2013). We henceforth assume that the non-

**Table 1.** Observation system characteristics[a].

| Observation system | Single sounding footprint size | Single $CH_4$ measurement precision | Visits per day |
|---|---|---|---|
| LEO | 7 km × 7 km | 0.6 % (10.8 ppb) | 1 |
| GEO | 3 km × 3 km | 0.6 % (10.8 ppb) | 4 |
| LEO+[b] | 7 km × 7 km | 0.42 % (7.6 ppb) | 1 |
| GEO×2 | 3 km × 3 km | 0.6 % (10.8 ppb) | 8 |
| GEO-Z1 | 3 km × 3 km | 0.6 % (10.8 ppb) | 4[c] |
| GEO-Z2 | 3 km × 3 km | 0.6 % (10.8 ppb) | 4[d] |

[a] LEO and GEO observation parameters are broadly consistent with TROPOMI and GEOCAPE simulations by Wecht et al. (2014); to simplify comparisons, we set GEO and LEO default single $CH_4$ sounding precision to 0.6 %. [b] Single measurement precision is a factor of $\sqrt{2}$ higher than LEO; this is the equivalent to doubling the visits per day for LEO. [c] 2 (6) visits per day in 0–50 percentile (50–100 percentile) cloud-cover areas; [d] 2 (10) visits per day in 0–75 percentile (75–100 percentile) cloud-cover areas.

wetland $CH_4$ contribution (namely fires and anthropogenic $CH_4$ sources) can be relatively well characterized using ancillary datasets and global inventories (Bloom et al., 2015; Turner et al., 2015, and references therein).

#### 2.3.1 LEO and GEO $CH_4$ observations

The advantage of LEO systems is a near-global coverage; for the TROPOMI mission $CH_4$ orbit and measurement parameters, this equates to a 1-day maximum revisit period globally. While a GEO system can only view a fixed area on the globe, revisit periods can be far shorter. To relate $CH_4$ observation requirements to current technological capabilities, we explore six OS configurations based on LEO and GEO OS parameters used to simulate the upcoming GEOCAPE and TROPOMI missions' observations in North America by Wecht et al. (2014) (Table 1). We note that, for regional $CH_4$ emission estimates, the GEO OS configurations are expected outperform LEO due to a larger data volume: the fixed viewing area permits multiple revisits per day (Wecht et al., 2014), and the smaller GEO footprint size typically leads to lower cloud contamination (Crisp et al., 2004). Our aim here is not to compare $CH_4$ emission estimates from LEO and GEO $CH_4$ retrievals. Rather, our aim is to determine whether $CH_4$ emission estimates from a range of LEO and GEO OS configurations are able meet the wetland process requirements outlined in Sect. 2.1.

Cloud cover is a major limiting factor in Amazon basin trace-gas retrievals. Mean March 2007 cloud cover is 89 % – ranging from 38 to 98 % at a $1^\circ \times 1^\circ$ resolution – throughout the Amazon River basin (based on MODIS cloud-cover data; Fig. B1). We quantify the data rejection due to cloud cover based on 1 km March 2007 MODIS cloud-cover data. Based on four MODIS cloud-cover flags, we categorize 1 km × 1 km cloud-cover observations into "cloud-contaminated" and "cloud-free" observations (see Appendix C). Any cloud-contaminated 3 km × 3 km (GEO) or 7 km × 7 km (LEO) $CH_4$ measurement footprints are rejected; i.e., all accepted footprints are 100 % "cloud-free".

To assess the relative importance of $CH_4$ measurement density in high cloud-cover areas, we test two additional geostationary configurations: "GEO-Z1" carries out two visits per day and six visits per day in the top 50 % cloudiest areas; "GEO-Z2" carries out 2 visits per day and 10 visits per day in the top 25 % cloudiest areas (we note that these two OSs would require targeting capabilities to optimize the sampling strategy over the cloudiest area of the basin). We further explore OS space by testing LEO with a $\sqrt{2}$ precision enhancement ("LEO+") and GEO with eight visits per day instead of four ("GEO×2").

#### 2.3.2 Cumulative $CH_4$ measurement precision

For each OS $\omega$ ("GEO","LEO", etc.), $\boldsymbol{O}^{\{L,\omega\}}$ is the cumulative $CH_4$ measurement precision at a $L \times L$ resolution. $\boldsymbol{O}^{\{L,\omega\}}$ is an $N \times 1$ array, where $N$ is the number of Amazon River basin grid cells at resolution $L \times L$. We derive the cumulative atmospheric $CH_4$ precision within each $L \times L$ grid cell $i$, $O_i^{\{L,\omega\}}$ as follows:

$$O_i^{\{L,\omega\}} = \frac{\sigma_\omega}{\sqrt{a\phi_i^{\{\omega\}} n^{\{\omega\}} L^2}}, \quad (1)$$

where $\sigma_\omega$ is the single observation precision (Table 1), $\phi_i^{\{\omega\}}$is the fraction of cloud-free observations at location $i$, $n^{\{\omega\}}$ is the number of observations per $km^2$ per month for OS $\omega$ (based on Table 1 values) and $a$ the fraction of accepted cloud-free $CH_4$ column retrievals (set to $a = 0.5$). The derivation of $\phi_i^{\{\omega\}}$ is based on MODIS 1 km cloud-cover data over the Amazon River basin in March 2007 (Appendix C). The square of the denominator in (1) corresponds to the number of cloud-free atmospheric column $CH_4$ measurements per $L \times L$ grid cell. For all OSs, $n^{\{\omega\}}$ is calculated assuming continuous basin-wide coverage at the single-sounding footprint resolution (see Table 1). We highlight that our formulation of cumulative $CH_4$ precision in Eq. (1) implies retrieved $CH_4$ errors are spatially and temporally uncorrelated.

#### 2.3.3 OS-retrieved $CH_4$ flux precision

We calculate the monthly retrieved $CH_4$ flux precision for OS $\omega$ at an $L \times L$ resolution – $F^{\{L,\omega\}}$ – based on $\boldsymbol{O}^{\{L,\omega\}}$ (Eq. 1). $F^{\{L,\omega\}}$ is a $N \times 1$ array, where $N$ is the number of Amazon basin grid cells at resolution $L \times L$. To calculate $\boldsymbol{F}^{\{L,\omega\}}$ we simulate an ensemble of 1000 retrieved $CH_4$ concentration vectors ($\boldsymbol{c}_{*,n}^{\{L,\omega\}}$ for $n = 1$–1000) over the Amazon River basin, where

$$\boldsymbol{c}_{*,n}^{\{L,\omega\}} = \boldsymbol{c}^{\{L,0\}} + \boldsymbol{N}(0,1) \circ \boldsymbol{O}^{\{L,\omega\}}. \quad (2)$$

$\boldsymbol{c}^{\{L,0\}}$ is a $N \times 1$ array of $L \times L$ gridded unperturbed $CH_4$ concentrations, and $\boldsymbol{N}(0,1)$ is an $N \times 1$ array of normally

distributed random numbers with mean zero and variance one ("$\circ$" denotes element-wise multiplication). We relate the concentrations $\boldsymbol{c}^{\{L,*\}}$ to the underlying $CH_4$ fluxes $\boldsymbol{f}^{\{L,*\}}$ as follows:

$$\boldsymbol{c}^{\{L,*\}} = \mathbf{A}^{\{L\}} \boldsymbol{f}^{\{L,*\}}, \tag{3}$$

where $\mathbf{A}^{\{L\}}$ is the atmospheric transport operator (the $N \times N$ matrix transforming fluxes to concentrations over the Amazon River basin domain) and $\boldsymbol{f}^{\{L,*\}}$ is an $N \times 1$ array of surface $CH_4$ fluxes. For the sake of brevity, we present a summary of $\mathbf{A}^{\{L\}}$ here and the complete derivation of $\mathbf{A}^{\{L\}}$ in Appendix D. We use a Lagrangian Particle Dispersion Model (LPDM: Uliasz, 1994; Lauvaux and Davis, 2014) to derive an "influence function" (or "column footprint") relating satellite-retrieved atmospheric $CH_4$ concentrations to surface fluxes (the inverse solution of the transport from the surface to higher altitudes) at the center of the study area. We simulate 30 km × 30 km $CH_4$ transport – $\mathbf{A}^{\{30\,\mathrm{km}\}}$ – by spatially translating the LPDM influence function throughout the domain. To assess the robustness of the LPDM approach, we also simulated $CH_4$ column mixing ratios over the Amazon River basin at 30 km using the Weather Research and Forecasting model (WRF v2.5.1; Skamarock and Klemp, 2008). The WRF model March 2007 Amazon River basin concentrations and the corresponding LPDM approximations are shown in Fig. D1. Finally, we used a Monte Carlo approach to statistically construct $\mathbf{A}^{\{L\}}$ based on $\mathbf{A}^{\{30\,\mathrm{km}\}}$. The LPDM, WRF and the Monte Carlo derivation of $A$ are fully described in Appendix D.

For each $L$, we simulate the flux uncertainty based on the inverse of $\mathbf{A}^{\{L\}}$, $(\mathbf{A}^{\{L\}})^{-1}$ and simulated $CH_4$ concentration vectors ($\boldsymbol{c}^{\{L,\omega\}}_{*,n}$, Eq. 2). For the sake of simplicity, we set all unperturbed concentrations – $\boldsymbol{c}^{\{L,0\}}$ in Eq. (2) – to be equal to zero, since these do not influence our subsequent derivation of $\boldsymbol{F}^{\{L,\omega\}}$. The $n$th retrieved flux estimate – $\boldsymbol{f}^{\{L,\omega\}}_{*,n}$ – is calculated as

$$\boldsymbol{f}^{\{L,\omega\}}_{*,n} = (\mathbf{A}^{\{L\}})^{-1} \boldsymbol{c}^{\{L,\omega\}}_{*,n}. \tag{4}$$

Finally, we calculate the flux precision $\boldsymbol{F}^{\{L,\omega\}}$ at grid cell $i$ as follows:

$$F^{\{L,\omega\}}_{i} = \mathrm{SD}\left(\boldsymbol{f}^{\{L,\omega\}}_{i,*}\right). \tag{5}$$

#### 2.3.4 Residual $CH_4$ bias simulation

Despite the implementation of $CH_4$ bias correction methods based on satellite $CH_4$ retrieval comparison against ground measurements of total column $CH_4$ (Parker et al., 2011), spatial structures in residual $CH_4$ biases are a key limiting factor in top-down $CH_4$ flux accuracy. Here we quantify the role residual $CH_4$ biases for each OS configurations. We simulate a retrieved pseudo-random $CH_4$ bias structure with a spatial correlation of $s = 100$ km and no temporal correlation, which is consistent with the likely first-order predictors of retrieved $CH_4$ residual biases (Worden et al., 2016). Here we simulate a range of pseudo-random bias distributions with standard deviations spanning $b = 0.5$–$50$ ppb. For each $b$, we calculate the bias-influenced flux uncertainty $\boldsymbol{F}^{\{L,\omega,b\}}$ based on Eqs. (4) and (5): to incorporate spatially correlated biases, we adapt Eq. (2) to derive the $CH_4$ concentration vector $\boldsymbol{c}'^{\{L,\omega,b\}}_{*,n}$ as

$$\boldsymbol{c}'^{\{L,\omega,b\}}_{*,n} = \boldsymbol{N}(0,1) \cdot \boldsymbol{O}^{\{L,\omega\}} + \boldsymbol{N}(0,1) \cdot b \cdot \frac{s}{L\sqrt{v}}, \tag{6}$$

where $b$ represents the standard deviation of the pseudo-random $CH_4$ bias and $v$ represents the number of visits per month; for bias errors correlated across spatial scales $s$, the scale factor $\frac{s}{L\sqrt{v}}$ accounts for the pseudo-random behavior of bias errors$b$at a monthly $L \times L$ resolution. We assess the role $CH_4$ biases on $\boldsymbol{F}^{\{L,\omega,b\}}$ for the LEO and GEO OS configurations at $L = \sim 333$ km.

## 3 Results and discussion

Cumulative $CH_4$ precision for mean monthly atmospheric column $CH_4$ measurements is 0.10–0.98 ppb for the LEO OS (Fig. 5, left) and 0.02–0.20 ppb for the GEO OS (Fig. 5, right). The lowest $CH_4$ concentration precision occurs in the eastern and central Amazon River basin. A crucial advantage of the smaller GEO OS footprint is the 88–148 % higher probability of cloud-free observations in the cloudiest regions of the Amazon River basin (Fig. B1); the probability of acquiring cloud-free observations in cloud-prone areas is further enhanced by the GEO OS ability to conduct multiple visits per day (see Eq. 1).

For $L = \sim 333$ km, median monthly retrieved $CH_4$ flux precision for the LEO OS (i.e., the median of $\boldsymbol{F}^{\{L,\omega\}}$) is 17.0 mg $CH_4$ m$^{-2}$ day$^{-1}$ (Fig. 6); increasing the single sounding retrieval precision by $\sqrt{2}$ (from 0.6 to 0.42 ppb) for LEO observations (LEO+) reduces the retrieved flux uncertainty to 11.9 mg $CH_4$ m$^{-2}$ day$^{-1}$. This uncertainty reduction is equivalent to a second LEO visit per day (see Table 1): the factor 3-to-10 lower uncertainties for cumulative GEO $CH_4$ concentrations (Fig. 5) lead to a 2.7 mg $CH_4$ m$^{-2}$ day$^{-1}$ median uncertainty in the retrieved flux (Fig. 6). Doubling the number of GEO visits per day (GEO×2 OS) reduces the retrieved flux uncertainty to 1.9 mg $CH_4$ m$^{-2}$ day$^{-1}$. GEO-Z1 and GEO-Z2 uncertainties (2.4 and 2.0 mg $CH_4$ m$^{-2}$ day$^{-1}$) are both lower than GEO. These results indicate that – despite a lower number of cloud-free observations – a higher observation density in the high cloud-cover areas of the Amazon basin (and lower observation density elsewhere) can be used to reduce the retrieved $CH_4$ flux uncertainty without increasing the number of observations per day. Based on the LEO OS, we anticipate that missions similar to the ESA TROPOMI observation configuration (Veefkind et al., 2012;

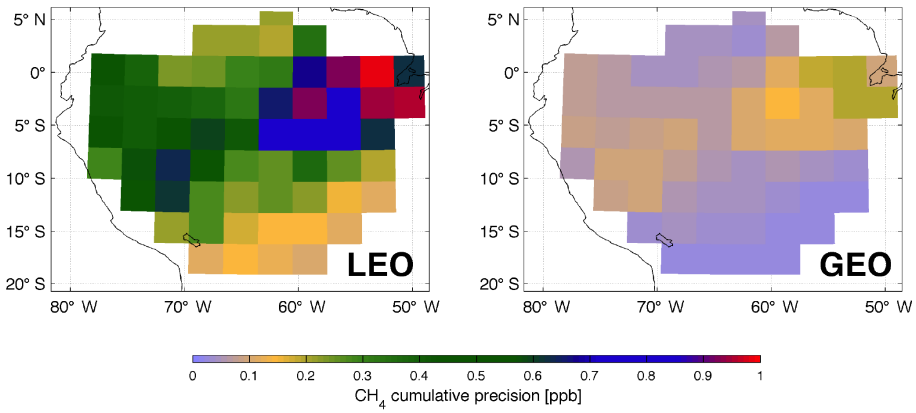


**Figure 5.** Retrieved monthly ∼ 333 km $CH_4$ cumulative precision (i.e., the combined precision of monthly-averaged $CH_4$ measurements) for LEO and GEO observing systems; the observing system configurations are described in Table 1.

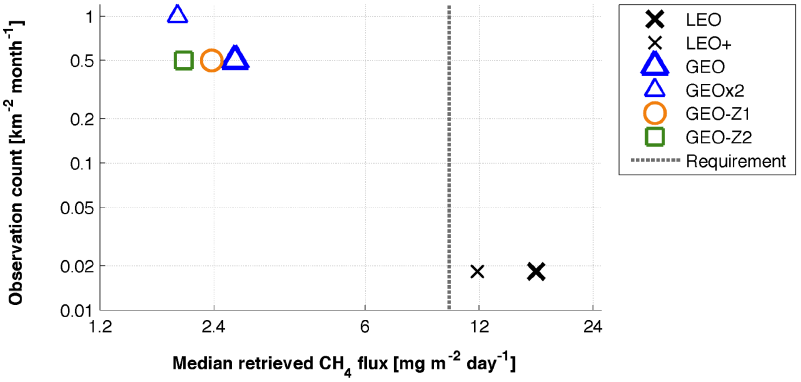


**Figure 6.** $CH_4$ observations density (observations per unit area; $y$ axis) vs. retrievable ∼ 333 km flux precision ($x$ axis) for six $CH_4$ observation systems (see Table 1 for details). The "observation density" includes all attempted $CH_4$ measurements, including accepted (cloud-free) and rejected (cloudy) observations.

Wecht et al., 2014) will lead to lower-than-required information content for Amazon wetlands and are unlikely to provide sufficient observational constraints to resolve the dominant $CH_4$ flux process controls.

Our bias $CH_4$ analysis (Fig. 7) indicates that GEO-retrieved $CH_4$ flux precisions at $L =\sim 333$ km are relatively unaffected by residual $CH_4$ biases $< 1$ ppb, while LEO-retrieved $CH_4$ flux precisions are relatively unaffected by residual $CH_4$ biases $< 5$ ppb. We find that the advantage of GEO $CH_4$ flux precision over LEO diminishes from almost 1 order of magnitude at residual $CH_4$ biases $< 1$ ppb, to roughly a factor of 2 for residual biases $> 20$ ppb. Here we assume a residual $CH_4$ bias correlation scale of 100 km (Sect. 2.3); based on Eq. (6), we expect a larger impact of residual $CH_4$ biases on OS-retrieved $CH_4$ flux precision for residual $CH_4$ bias correlation lengths $> 100$ km or for temporally correlated $CH_4$ biases. Overall, the relative advantage of GEO over LEO OSs is contingent on both the cumulative $CH_4$ precision (Fig. 5) as well as the anticipated spatiotemporal structure of residual $CH_4$ bias.

Estimates of fluxes at $L = 150$–$990$ km show that median GEO-retrieved $CH_4$ flux uncertainty is consistently a factor of ∼ 5 lower than the median LEO-retrieved $CH_4$ flux uncertainty (Fig. 8); for a 10 ppb residual pseudo-random bias, the median GEO-retrieved flux uncertainty is consistently a factor of ∼ 3 lower than LEO-retrieved flux uncertainty. GEO-derived $CH_4$ fluxes meet the both the precision and resolution requirements for $L =\sim 180$–$333$ km; for a 10 ppb residual bias, GEO-derived $CH_4$ fluxes meet both requirements at $L =\sim 280$–$333$ km. At the expense of the resolution requirement, both GEO simulations meet the precision requirements for all $L \geq\sim 333$ km. Unbiased median LEO-derived $CH_4$ fluxes meet the precision requirements at $L > 500$ km; LEO-derived $CH_4$ fluxes with a 10 ppb pseudo-random bias meet the precision requirement at $L > 800$ km and partially meet the precision requirement for $550\,\text{km} > L > 800$ km.

In our analysis we have assumed (i) no systematic biases in our atmospheric inversion simulation and (ii) perfectly known boundary conditions. Significant systematic atmospheric $CH_4$ retrieval and transport model biases can un-

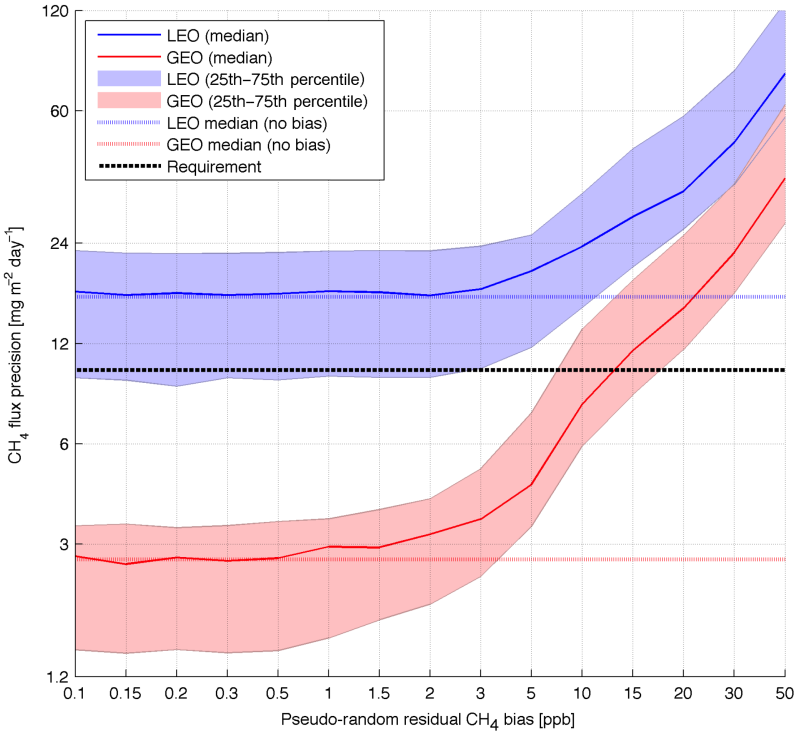


**Figure 7.** Retrieved GEO and LEO flux precision for $L = \sim 333$ km with modeled pseudo-random residual bias error. See Table 1 for details on GEO and LEO $CH_4$ observing systems.

dermine the enhanced accuracy of geostationary OSs. For example, we find that our LPDM-derived transport operator yields a conservative estimate of the monthly mean $CH_4$ gradient across the domain relative to the WRF model simulation (Appendix D; Fig. D1). We assess the sensitivity of our results to a factor of 1.5 increase in the LPDM-derived transport operator ($A^{\{L\}}$); OS $CH_4$ flux precision results exhibit an inversely proportional response, corresponding to a $\sim 33\,\%$ uncertainty reduction (median GEO flux precision of 1.8 mg $CH_4$ $m^{-2}$ $day^{-1}$ and a LEO precision of 11.3 mg $CH_4$ $m^{-2}$ $day^{-1}$). GEO missions are likely to provide a higher volume of observations at the boundaries of the observation domain, relative to LEO OS: therefore, boundary conditions are likely to reinforce the potential of GEO OS compared to LEO. We recognize that further efforts are required to fully assess the role of seasonal transport variability, transport errors, boundary condition assumptions and atmospheric $CH_4$ bias structures on the accuracy of GEO and LEO $CH_4$ flux retrievals.

We note that a limiting factor in our analysis is the lack of data constraints on diurnal cloud-cover variability (since the MODIS cloud-cover dataset does not provide diurnal constraints). The March 2007 ERA-Interim monthly mean 3 h cloud-cover dataset indicates a 7–80 % (median 29 %) coefficient of variation of cloud-free fraction diurnal variability throughout the Amazon basin. Given the nonlinear sensitivity of data yield to synoptic cloud cover (Fig. B1), the cloud-free fraction coefficient of variation may amount to an important component in assessing and optimizing the performance of LEO and GEO OSs over the Amazon basin, as well as other high cloud-cover regions across the globe.

Our $CH_4$ flux resolution requirement (monthly $L = \sim 333$ km $CH_4$ flux retrievals) is derived based on an assessment of carbon and hydrological autocorrelation scales across the Amazon River basin. Although our sensitivity analysis (Fig. 8) shows that GEO can potentially distinguish between the hypothesized $CH_4$ emission scenarios at $L > \sim 333$ km, we anticipate that additional biogeochemical investigations – such as the second-order interactions between carbon and hydrological drivers on wetland $CH_4$ emissions – would likely be increasingly challenging at coarser resolutions. We recognize that our resolution requirement and our quantification of correlation scales is specific to our study region: for example, quantification of greenhouse gas measurement requirements for finer-scale studies would yield a unique set of requirements, and supporting analyses may require higher-resolution datasets. Our approach provides the means to examine trade-offs between spatial and temporal resolutions. For example, further analyses can be conducted to establish the space–time trade-offs to optimize biogeochemical investigations and process uncertainty reduction. We also note that GEO OSs provide unprecedented volume of observations: the enhanced sampling approach can potentially be used at shorter timescales to optimally resolve

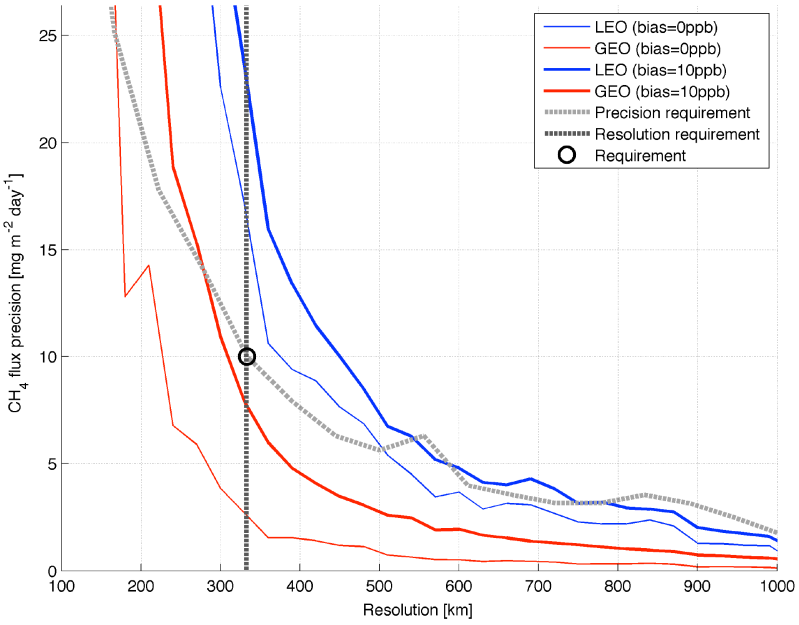


**Figure 8.** Median retrieved LEO and GEO $CH_4$ fluxes for $L = 150$–$990$ km; the dashed lines indicate precision and resolution requirements. See Table 1 for details on GEO and LEO $CH_4$ observing systems. The bias value of 10 ppb indicates modeled systematic $CH_4$ measurement biases with 100 km spatial correlations (see Sect. 2.3).

source and transport patterns. This approach could be particularly useful in instances when wetland $CH_4$ emissions are densely focused in space or time. Finally, we highlight the potential for combining multiple OSs (e.g., LEO and GEO systems) to optimally constrain $CH_4$ fluxes and biogeochemical process controls; the potential of OS synergies undoubtedly requires further investigation.

In contrast to our approach, $CH_4$ flux uncertainty requirements can alternatively be derived by quantifying process-based wetland $CH_4$ emission model uncertainty (Melton et al., 2013) or by characterizing the $CH_4$ flux uncertainty stemming from wetland $CH_4$ model parametric uncertainty (Bloom et al., 2012). An advantage of model-based requirements is the ability to assess $CH_4$ flux uncertainties associated with the complex interactions between wetland $CH_4$ processes (e.g., Riley et al., 2011). Prior information on the magnitude and variability of fluxes can also be introduced (e.g., in a Bayesian atmospheric transport and chemistry inversion framework) to reassess posterior uncertainty estimates.

However, as outlined in Sect. 2.1, large unknowns preside over the processes governing the spatial and temporal variability of wetland $CH_4$ fluxes. Moreover, wetland $CH_4$ models often exhibit structural similarities (Melton et al., 2013); for example, wetland $CH_4$ emission models (Melton et al., 2013) suggest major $CH_4$ emissions along the main stem of the Amazon River (Fig. 1). Since model spatiotemporal $CH_4$ flux variations – and their associated processes – have not been adequately assessed due to insufficient in situ measurements (particularly in the tropics), the introduction of prior spatial and temporal correlations in wetland $CH_4$ flux estimates would hinder the potential to independently investigate biogeochemical process controls on wetland $CH_4$ emissions. To our knowledge, our analysis provides a first quantification of the OS requirements for confronting prior knowledge on $CH_4$ fluxes at a process-relevant resolution.

## 4 Concluding remarks

Quantitative knowledge of biogeochemical processes controlling biosphere–atmosphere greenhouse gas fluxes remains highly uncertain. Optimally designed satellite greenhouse gas OSs can potentially resolve the processes controlling critical boreal and tropical greenhouse gas fluxes. In this study, we have characterized a satellite OS able to resolve the principal process controls on Amazon basin wetland $CH_4$ emissions. Conventional low-earth orbit satellite missions will likely be unable to resolve Amazon wetland $CH_4$ emissions at a process-relevant scale and precision. Observation density in time and space, and its reduction by cloud cover are the major limiting factors. Increasing the number of daily $CH_4$ measurements in cloudy regions at the expense of other measurements can further reduce the retrieved $CH_4$ flux precision from geostationary satellite $CH_4$ measurements. OSSEs based on reducing process uncertainty can inform observation requirements for future greenhouse gas satellite missions in a far more targeted way than simply quantifying overall flux uncertainty reduction for a given OS.

## 5 Data availability

The Surface WAter Microwave Product Series inundation dataset (described by Schroeder et al., 2015) was obtained from http://wetlands.jpl.nasa.gov (accessed on 5 June 2014); the land surface inundation dataset described by Prigent et al (2012) was obtained from http://noaacrest.org/rscg/ (accessed on 20 May 2014). TRMM 3B43 (V7) precipitation data are available at http://mirador.gsfc.nasa.gov (accessed on 12 May 2014). The gross primary production dataset (described by Jung et al., 2009) was obtained from http://bgc-jena.mpg.de (accessed 15 June 2012). The Harmonized World Soil Database soil carbon dataset is available at http://esdac.jrc.ec.europa.eu (accessed on 23 April 2014). European Centre for Medium-Range Weather Forecasts reanalysis (ECMWF ERA-Interim) synoptic monthly means were downloaded from http://apps.ecmwf.int (accessed on 7 April 2015).

## Appendix A: Correlation lengths

All datasets described in Sect. 2.2 were aggregated to a common $0.5° \times 0.5°$ resolution. For each process control dataset, we derive the Moran's I spatial autocorrelation coefficient ($r_{MI}$) at an $L \times L$ resolution, where $L = 0.5, 1, 1.5, \ldots, 10°$. For every $L$ we aggregated the dataset to $L \times L$ resolution. To determine whether the derived $r_{MI}$ are significant relative to the null hypothesis, we repeat the Moran's I derivation 2000 times for normally distributed random numbers (in the place of the $L \times L$ gridded dataset), which together statistically represent the Moran's I distribution ($\boldsymbol{R}_{MI}$) for statistically insignificant spatial correlation. When $r_{MI} > \text{median}(\boldsymbol{R}_{MI})$, the $r_{MI}$ $p$ value is twice the fraction of instances where $\boldsymbol{R}_{MI} > r_{MI}$; when $r_{MI} < \text{median}(\boldsymbol{R}_{MI})$, the $r_{MI}$ $p$ value is twice the fraction of instances where $\boldsymbol{R}_{MI} < r_{MI}$. A $p$ value $\geq 0.05$ indicates that the null hypothesis cannot be rejected with a 95 % confidence.

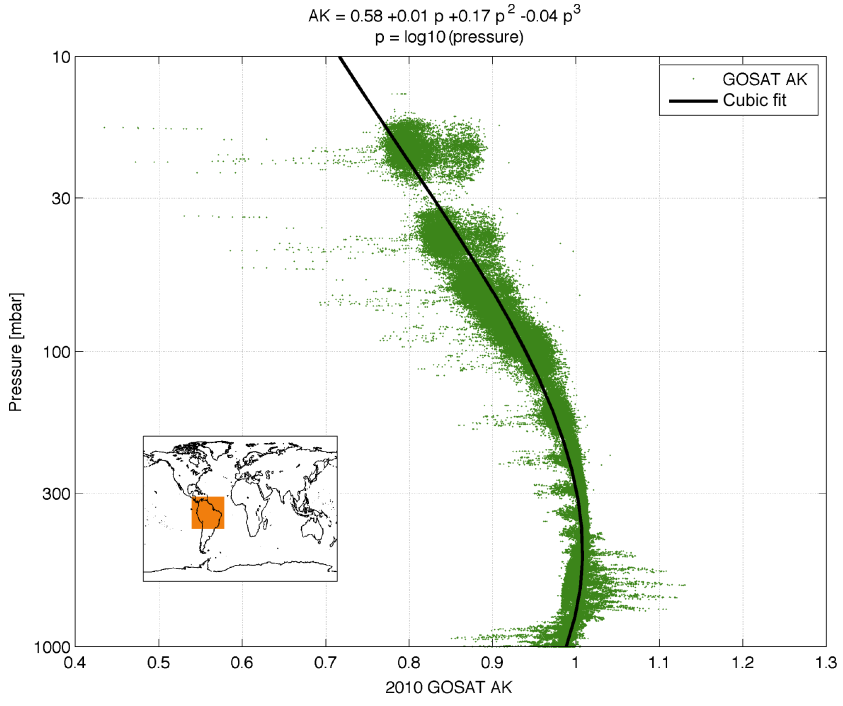


**Figure A1.** January to December 2010 GOSAT averaging kernels (AKs) for the broader Amazon region (green dots). The black line denotes the AK cubic fit (w.r.t. pressure $p$; equation shown at the top of the figure). This AK was used to vertically weight the LPDM footprint and sample WRF $CH_4$ concentrations (see Appendix D).

## Appendix B: Spatial and temporal wetland $CH_4$ emission hypotheses

### B1 Detectability of wetland $CH_4$ hypotheses

Based on the four carbon and three hydrological proxies (see Sect. 2.2), we formulate spatial and temporal wetland $CH_4$ emission hypotheses (henceforth **S** and **T** respectively) – at a monthly $\sim$333 km resolution – and determine our ability to statistically distinguish between these at a range of retrieved $CH_4$ flux precisions ($p = 1$–$100\,\mathrm{mg\,m^{-2}\,day^{-1}}$). For all $S$ we prescribe temporally constant $CH_4$ emissions and for $T$ we annually normalize mean annual emissions to $12\,\mathrm{mg\,m^{-2}\,day^{-1}}$ within each $\sim 333\,\mathrm{km} \times 333\,\mathrm{km}$ area. For both **S** and **T** we also include a "no variability" scenario, where all emissions in space and time are $12\,\mathrm{mg\,m^{-2}\,day^{-1}}$. We note that by minimizing the variability of each hypothesis to a single temporal or spatial variable, we effectively assume a "worst-case" scenario for the detectability **S** and **T** hypotheses relative to the null hypothesis.

For hypothesized process control $h$ we derive the temporal wetland $CH_4$ emission hypothesis $\mathbf{T}_{*,*,h}$, as

$$T_{x,t,h} = s_x\, P_{x,t,h}, \tag{B1}$$

where $P_{x,t,h}$ represents the hypothesized process control $h$ at location $x$ and time $t$, and $s_x$ is a scaling factor such that $\overline{\boldsymbol{T}_{x,*,h}} = 12\,\mathrm{mg\,m^{-2}\,day^{-1}}$. For the temporal hypotheses we omit the soil carbon and carbon stock proxies, as these datasets are not temporally resolved. Each spatial hypothesis $\mathbf{S}_{*,*,h}$ is defined as

$$S_{x,t,h} = s\,\overline{\boldsymbol{P}_{x,*,h}}, \tag{B2}$$

where $s$ is a scaling factor such that $\overline{S_{*,t,h}} = 12\,\mathrm{mg\,m^{-2}\,day^{-1}}$. For each hypothesis $h$ and each precision $p$ we simulate retrieved $CH_4$ fluxes $F_{x,t,h,p}$ as

$$F_{x,t,h,p} = H_{x,t,h} + N(0,1)\cdot p, \tag{B3}$$

where $H_{x,t,h}$ is the spatial or temporal hypothesis $CH_4$ flux ($T_{x,t,h}$ or $S_{x,t,h}$) and $N(0,1)$ is a normally distributed number with mean 0 and variance of 1. For each $h$, we compare $\mathbf{F}_{*,*,h,p}$ against all hypothesized process controls $h'$ as follows:

$$J_{h,h',p} = \sum_{x,t} (F_{x,t,h,p} - H_{x,t,h'})^2. \tag{B4}$$

We repeat the derivation of $J$ 500 times, and we define the detectability confidence $C_{h,p}$ as the percentage of times where $J_{h,h,p} = \min(\boldsymbol{J}_{h,*,p})$; the min() function denotes the minimum of all $\boldsymbol{J}_{h,*,p}$ elements. In summary, $C_{h,p}$ is the probability of correctly distinguishing a hypothesized wetland $CH_4$ process control $h$ from alternative wetland $CH_4$ process controls when wetland $CH_4$ fluxes are retrieved with precision $p$. $C_{h,p}$ values for spatial and temporal wetland $CH_4$ hypotheses are summarized in Fig. 4. We henceforth define a wetland $CH_4$ hypothesis as "distinguishable" from alternative hypotheses at precision $p$ when $C_{h,p} > 95\,\%$.

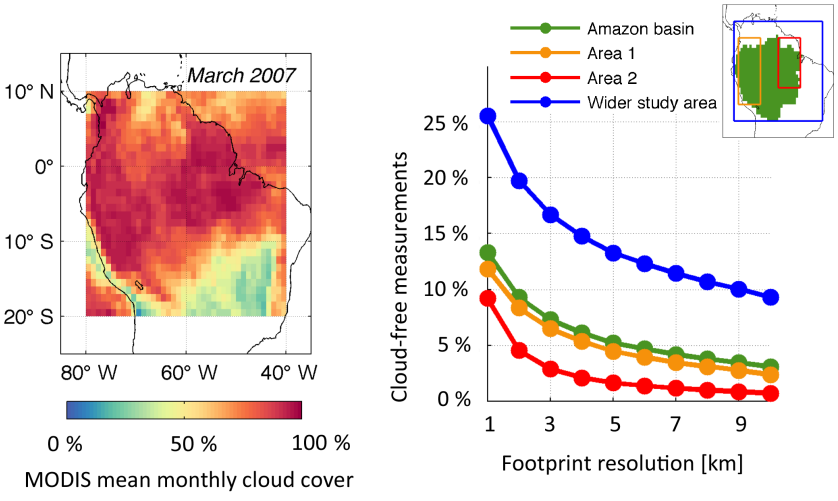


**Figure B1.** Left: March 2007 mean MODIS cloud cover aggregated to $1^\circ \times 1^\circ$. Right: summary of March 2007 cloud-free observations vs. footprint size for the broader study area, the Amazon River basin and two subregions (eastern and western Amazon River basin).

## Appendix C: MODIS cloud cover

The MODIS cloud-cover analysis was performed based on the MOD06_L2 1 km cloud mask product (downloaded from http://modis.gsfc.nasa.gov). We consider "probably cloudy" and "cloudy" 1 km × 1 km pixel flags as cloud-covered areas (CC = 1) and the remaining pixel flag categories ("probably clear" and "clear") as cloud-free areas (CC = 0): here we assume that the statistical patterns of cloud-cover across the Amazon domain remain well characterized when assigning "probably clear" and "probably cloudy" pixels to the "cloud-free" and "cloud-covered" categories. We aggregate the 1 km data to $N$ km × $N$ km ($N$ is the OS footprint resolution; GEO $N = 3$ km; LEO $N = 7$ km; see Table 1) to calculate the number of cloud-free $N$ km × $N$ km areas within each MODIS cloud-cover scene. The monthly fraction of cloud-free observations $\phi_i^{\{\omega\}}$(see Eq. 1) is calculated by deriving the ratio of cloud-free to total $N$ km × $N$ km areas within each $L \times L$ area. A regional summary of the observation yields (percent of cloud-free $N$ km × $N$ km areas) for a range of footprint resolutions ($N$ = 1–10 km) is shown in Fig. B1.

## Appendix D: Atmospheric transport operator

For $L$ = 150–990 km, we derive the $N \times N$ atmospheric transport operator $\mathbf{A}^{\{L\}}$ for $L \times L$ resolution fluxes based on $N$ random $CH_4$ flux vectors ($\mathbf{f}'^{\{L\}}$) and their corresponding concentrations ($\mathbf{c}'^{\{L\}}$): $\mathbf{f}'^{\{L\}}$ and $\mathbf{c}'^{\{L\}}$ are $N \times N$ arrays, where each column of $\mathbf{f}'^{\{L\}}$ is a vector of randomly sampled $CH_4$ fluxes throughout the domain, and each column in $\mathbf{c}'^{\{L\}}$ is a vector of the corresponding $CH_4$ concentrations. $\mathbf{A}^{\{L\}}$ is derived as

$$\mathbf{A}^{\{L\}} = \left(\mathbf{f}'^{\{L\}}\right)^{-1} \mathbf{c}'^{\{L\}}. \quad \text{(D1)}$$

For each $n$, random $CH_4$ fluxes at grid cell $i$ are derived as $f'^{\{L\}}_{i,n} = R(0,1)$, where $R(0,1)$ is a random number sampled from a normal distribution with mean zero and variance 1. Atmospheric concentrations are firstly simulated at resolution $L_0$ = 30 km; the fluxes $\boldsymbol{f}'^{\{L\}}_{*,n}$ are downscaled to $L_0 \times L_0$ resolution ($\boldsymbol{f}'^{\{L_0\}}_{*,n}$). For each 30 km × 30 km grid cell $i$, the mean atmospheric $CH_4$ concentration $c'^{\{L_0\}}_{i,n}$ is calculated as

$$c'^{\{L_0\}}_{i,n} = \boldsymbol{I}_i \boldsymbol{f}'^{\{L_0\}}_{*,n}, \quad \text{(D2)}$$

where $f^{\{L_0\}}_{*,n}$ is the $N \times 1$ array of $CH_4$ fluxes and $\boldsymbol{I}_i$ is the $N \times 1$ influence function array for grid cell $i$. We derive $\boldsymbol{I}_i$ using an LPDM (Uliasz, 1994). The influence function derivation (i.e., the column sensitivity to the surface fluxes) is described in Lauvaux and Davis (2014). The influence function was computed for an averaged column observation in the model of the simulation domain, for every hour of March 2007. The inverse calculation of surface fluxes requires the use of the adjoint of the transport at the mesoscale (∼ 2000 km). Here, we only simulated the fraction of the column influenced by surface fluxes. We assume boundary conditions are well constrained by satellite and surface network measurements; therefore, only the first 6 km of the column was described by the particles released backward in the model.

To simulate total column $CH_4$ retrieval influence functions, we incorporate a mean GOSAT $CH_4$ retrieved averaging kernel (Parker et al., 2011) for the Amazon River basin region (Fig. A1). To minimize the computational cost of simulating atmospheric transport, we (i) derive the influence function for the center of the domain ($\boldsymbol{I}_0$; lat = 4.9° S and long = 63.8° W) and (ii) we derive $I_i$ by spatially translating $\boldsymbol{I}_0$ to grid cell $i$ latitude and longitude coordinates. Finally, we derive mean $L \times L$ resolution concentrations used in Eq. (C1), ($\boldsymbol{c}'^{\{L\}}_{*,n}$), based on the spatial aggregation of $L_0 \times L_0$ resolution concentrations $\boldsymbol{c}'^{\{L_0\}}_{*,n}$.

To assess the viability of our approach, we simulate March 2007 $L_0 \times L_0$ atmospheric concentrations – based on $\boldsymbol{f}^{\{L_0,0\}}$, where for $i = 1-N$, $f_i^{\{L_0,0\}} = 12\,\mathrm{mg\,m^{-2}\,day^{-1}}$ – throughout the Amazon River basin domain using (a) Eq. (D2) and (b) WRF $CH_4$ atmospheric transport model. In the WRF model, $\boldsymbol{f}^{\{L_0,0\}}$ was coupled to the atmospheric model through the chemistry modules (WRF-Chem) for passive tracers, as described in Lauvaux et al. (2012). The physics configuration of the model used Mellor–Yamada–Nakanishi–Niino scheme for the planetary boundary layer (Nakanishi and Niino, 2004), the NOAH land surface model (Pan and Mahrt, 1987), the WSM-5 microphysics scheme (Hong et al., 2004) and the Kain–Fritsch cumulus parameterization (Kain, 2004). The meteorological driver data from the Global Forecasting System (FNL) analysis products at 1° × 1° resolution were used at the boundaries of the simulation domain. The simulation domain spans 120 × 100 $L_0 \times L_0$ grid points and 60 vertical levels to describe the atmospheric column up to 50 hPa. The atmospheric column was extracted from the surface to the top of the modeled atmosphere, which represents about 90 % of the total air mass. A dilution factor of 0.9 was used to compensate for the partial model column.

The LPDM approach emulates the large-scale WRF $CH_4$ enhancement ($r^2 = 0.85$ see Fig. D1); the smoothing effect is due to the use of a single footprint throughout the entire domain. Mean $CH_4$ concentrations based on our approach (Eq. D2) and WRF are 15.23 and 17.42 $CH_4$ ppb respectively. The gradient of $CH_4$ between the northeastern and southwestern subregions for our approach (Eq. D2) and WRF are 13.14 and 17.24 $CH_4$ ppb respectively; the delineation of the northeastern and southwestern domain is shown in Fig. D1.

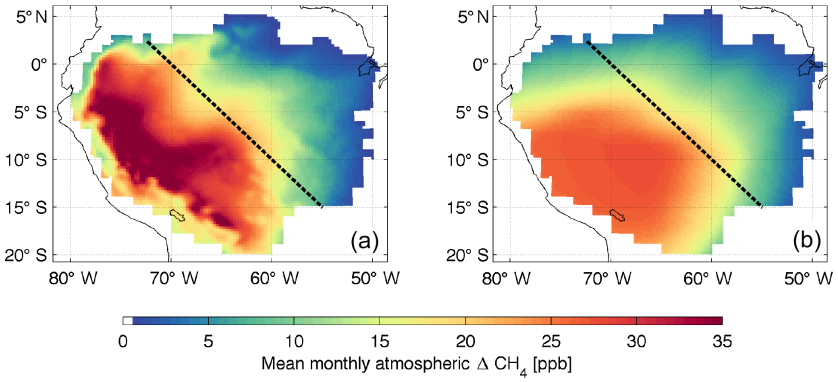


**Figure D1.** March 2007 simulations of atmospheric $CH_4$ concentration enhancements – based on 12 mg $m^{-2}$ $day^{-1}$ fluxes throughout the Amazon basin – derived using the WRF atmospheric transport model **(a)** and the LPDM influence function approach **(b)**. The dashed line denotes our delineation of "northeast Amazon basin" and "southwest Amazon basin" regions (see Appendix C).

*Acknowledgements.* The research was carried out at the Jet Propulsion Laboratory, California Institute of Technology, under a contract with the National Aeronautics and Space Administration.

Edited by: C. Gerbig
Reviewed by: two anonymous referees

## References

Andrews, A. E., Kofler, J. D., Trudeau, M. E., Williams, J. C., Neff, D. H., Masarie, K. A., Chao, D. Y., Kitzis, D. R., Novelli, P. C., Zhao, C. L., Dlugokencky, E. J., Lang, P. M., Crotwell, M. J., Fischer, M. L., Parker, M. J., Lee, J. T., Baumann, D. D., Desai, A. R., Stanier, C. O., De Wekker, S. F. J., Wolfe, D. E., Munger, J. W., and Tans, P. P.: $CO_2$, CO, and $CH_4$ measurements from tall towers in the NOAA Earth System Research Laboratory's Global Greenhouse Gas Reference Network: instrumentation, uncertainty analysis, and recommendations for future high-accuracy greenhouse gas monitoring efforts, Atmos. Meas. Tech., 7, 647–687, doi:10.5194/amt-7-647-2014, 2014.

Baccini, A., Goetz, S. J., Walker, W. S., Laporte, N. T., Sun, M., Sulla-Menashe, D., Hackler, J., Beck, P. S. A., Dubayah, R., Friedl, M. A., Samanta, S., and Houghton, R. A.: Estimated carbon dioxide emissions from tropical deforestation improved by carbon-density maps, Nat. Climate Change, 2, 182–185, doi:10.1038/nclimate1354, 2012.

Bacastow, R. B., Adams, J. A., Keeling, C. D., Moss, D. J., Whorf, T. P., and Wong, C. S.: Atmospheric carbon dioxide, the Southern Oscillation, and the weak 1975 El Niño, Science, 210, 66–68, doi:10.1126/science.210.4465.66, 1980.

Basso, L. S., Gatti, L. V., Gloor, M., Miller, J. B., Domingues, L. G., Correia, C. S., and Borges, V. F.: Seasonality and interannual variability of $CH_4$ fluxes from the eastern Amazon Basin inferred from atmospheric mole fraction profiles, J. Geophys. Res.-Atmos., 121, 168–184, doi:10.1002/2015JD023874, 2016.

Beer, C., Reichstein, M., Tomelleri, E., Ciais, P., Jung, M., Carvalhais, N., Rodenbeck, C., Arain, M. A., Baldocchi, D., Bonan, G. B., Bondeau, A., Cescatti, A., Lasslop, G., Lindroth, A., Lomas, M., Luyssaert, S., Margolis, H., Oleson, K. W., Roupsard, O., Veenendaal, E., Viovy, N., Williams, C., Woodward, F. I., and Papale, D.: Terrestrial Gross Carbon Dioxide Uptake: Global Distribution and Covariation with Climate, Science, 329, 834–838, doi:10.1126/Science.1184984, 2010.

Bergamaschi, P., Houweling, S., Segers, A., Krol, M., Frankenberg, C., Scheepmaker, R. A., Dlugokencky, E., Wofsy, S. C., Kort, E. A., Sweeney, C., Schuck, T., Brenninkmeijer, C., Chen, H., Beck, V., and Gerbig, C.: Atmospheric $CH_4$ in the first decade of the 21st century: Inverse modeling analysis using SCIAMACHY satellite retrievals and NOAA surface measurements, J. Geophys. Res., 118, 7350–7369, doi:10.1002/jgrd.50480, 2013.

Bloom, A. A., Palmer, P. I., Fraser, A., Reay, D. S., and Frankenberg, C.: Large-Scale Controls of Methanogenesis Inferred from Methane and Gravity Spaceborne Data, Science, 327, 322–325, doi:10.1126/Science.1175176, 2010.

Bloom, A. A., Palmer, P. I., Fraser, A., and Reay, D. S.: Seasonal variability of tropical wetland $CH_4$ emissions: the role of the methanogen-available carbon pool, Biogeosciences, 9, 2821–2830, doi:10.5194/bg-9-2821-2012, 2012.

Bloom, A. A., Worden, J., Jiang, Z., Worden, H., Kurosu, T., Frankenberg, C., and Schimel, D.: Remote sensing constraints on South America fire traits by Bayesian fusion of atmospheric and1140 surface data, Geophys. Res. Lett., 42, 1268–1274, doi:10.1002/2014GL062584, 2015.

Bloom, A. A., Exbrayat, J.-F., van der Velde, I. R., Feng, L., and Williams, M.: The decadal state of the terrestrial carbon cycle: Global retrievals of terrestrial carbon allocation, pools, and residence times, P. Natl. Acad. Sci. USA, 113, 1285–1290, doi:10.1073/pnas.1515160113, 2016.

Bousquet, P., Ringeval, B., Pison, I., Dlugokencky, E. J., Brunke, E.-G., Carouge, C., Chevallier, F., Fortems-Cheiney, A., Frankenberg, C., Hauglustaine, D. A., Krummel, P. B., Langenfelds, R. L., Ramonet, M., Schmidt, M., Steele, L. P., Szopa, S., Yver, C., Viovy, N., and Ciais, P.: Source attribution of the changes in atmospheric methane for 2006–2008, Atmos. Chem. Phys., 11, 3689–3700, doi:10.5194/acp-11-3689-2011, 2011.

Bousserez, N., Henze, D. K., Rooney, B., Perkins, A., Wecht, K. J., Turner, A. J., Natraj, V., and Worden, J. R.: Constraints on methane emissions in North America from future geostationary remote-sensing measurements, Atmos. Chem. Phys., 16, 6175–6190, doi:10.5194/acp-16-6175-2016, 2016.

Braswell, B. H., Schimel, D. S., Linder, E., and Moore, B. I. I. I.: The response of global terrestrial ecosystems to interannual temperature variability, Science, 278, 870–873, doi:10.1126/science.278.5339.870, 1997.

Butz, A., Guerlet, S., Hasekamp, O., Schepers, D., Galli, A., Aben, I., Frankenberg, C., Hartmann, J.-M., Tran, H., Kuze, A., Keppel-Aleks, G., Toon, G., Wunch, D., Wennberg, P., Deutscher, N., Griffith, D., Macatangay, R., Messerschmidt, J., Notholt, J., and Warneke, T.: Toward accurate $CO_2$ and $CH_4$ observations from GOSAT, Geophys. Res. Lett., 38, L14812, doi:10.1029/2011GL047888, 2011.

Butz, A., Galli, A., Hasekamp, O., Landgraf, J., Tol, P., and Aben, I.: TROPOMI aboard Sentinel-5 Precursor: Prospective performance of $CH_4$ retrievals for aerosol and cirrus loaded atmospheres, Remote Sens. Environ., 120, 267–276, doi:10.1016/j.rse.2011.05.030, 2012.

Caldararu, S., Palmer, P. I., and Purves, D. W.: Inferring Amazon leaf demography from satellite observations of leaf area index, Biogeosciences, 9, 1389–1404, doi:10.5194/bg-9-1389-2012, 2012.

Chave, J., Navarrete, D., Almeida, S., Álvarez, E., Aragão, L. E. O. C., Bonal, D., Châtelet, P., Silva-Espejo, J. E., Goret, J.-Y., von Hildebrand, P., Jiménez, E., Patiño, S., Peñuela, M. C., Phillips, O. L., Stevenson, P., and Malhi, Y.: Regional and seasonal patterns of litterfall in tropical South America, Biogeosciences, 7, 43–55, doi:10.5194/bg-7-43-2010, 2010.

Chen, Y., Randerson, J. T., and Morton, C. D.: Tropical North Atlantic ocean-atmosphere interactions synchronize forest carbon losses from hurricanes and Amazon fires, Geophys. Res. Lett., 42, 6462–6470, doi:10.1002/2015GL064505, 2015.

Cox, P. M., Pearson, D., Booth, B. B., Friedlingstein, P., Huntingford, C., Jones, C. D., and Luke, C. M.: Sensitivity of tropical carbon to climate change constrained by carbon dioxide variability, Nature, 494, 341–344, doi:10.1038/nature11882, 2013.

Crevoisier, C., Nobileau, D., Fiore, A. M., Armante, R., Chédin, A., and Scott, N. A.: Tropospheric methane in the tropics – first year

from IASI hyperspectral infrared observations, Atmos. Chem. Phys., 9, 6337–6350, doi:10.5194/acp-9-6337-2009, 2009.

Crisp, D., Atlas, R. M., Breon, F.-M., Brown, L. R., Burrows, J. P., Ciais, P., Connor, B. J., Doney, S. C., Fung, I. Y., Jacob, D. J., Miller, C. E., O'Brien, D., Pawson, S., Randerson, J. T., Rayner, P., Salawitch, R. J., Sander, S. P., Sen, B., Stephens, G. L., Tans, P. P., Toon, G. C., Wennberg, P. O., Wofsy, S. C., Yung, Y. L., Kuang, Z., Chudasama, B., Sprague, G., Weiss, B., Pollock, R., Kenyon, D., and Schroll, S.: The Orbiting Carbon Observatory (OCO) mission, Adv. Space Res., 34, 700–709, doi:10.1016/j.asr.2003.08.062, 2004.

Devol, A. H., Richey, J. E., Forsberg, B. R., and Martinelli, L. A.: Seasonal dynamics in methane emissions from the Amazon River floodplain to the troposphere, J. Geophys. Res., 95, 16417–16426, doi:10.1029/JD095iD10p16417, 1990.

Frankenberg, C., Bergamaschi, P., Butz, A., Houweling, S., Meirink, J. F., Notholt, J., Petersen, A. K., Schrijver, H., Warneke, T., and Aben, I.: Tropical methane emissions: A revised view from SCIAMACHY onboard ENVISAT, Geophys. Res. Lett., 35, L15811, doi:10.1029/2008GL034300, 2008.

Franklin, J., Serra-Diaz, J. M., Syphard, A. D., and Regan, H. M.: Global change and terrestrial plant community dynamics, P. Natl. Acad. Sci. USA, 113, 3725–3734, doi:10.1073/pnas.1519911113, 2016

Fung, I., John, J., Lerner, J., Matthews, E., Prather, M., Steele, L. P., and Fraser, P. J.: Three-dimensional model synthesis of the global methane cycle, J. Geophys. Res., 96, 13033–13065, doi:10.1029/91JD01247, 1991.

Friedlingstein, P., Meinshausen, M., Arora, V. K., Jones, C. D., Anav, A., Liddicoat, S. K., and Knutti, R.: Uncertainties in CMIP5 climate projections due to carbon cycle feedbacks, J. Climate, 27, 511–526, doi:10.1175/JCLI-D-12-00579.1, 2013.

Gurney, K. R., Baker, D., Rayner, P., Denning, S., Law, R., Bousquet, P., Bruhwiler, L., Chen, Y. H., Ciais, P., Fung, I., Heimann, M., John, J., Maki, T., Maksyutov, S., Peylin, P., Prather, M., Pak, B., and Taguchi, S.: Interannual variations in continental-scale net carbon exchange and sensitivity to observing networks estimated from atmospheric $CO_2$ inversions for the period 1980–2005, Global Biogeochem. Cy., 22, GB3025, doi:10.1029/2007GB003082, 2008.

Hong, S., Dudhia, J., and Chen, S.: A revised approach to ice microphysical processes for the bulk parameterization of clouds and precipitation, Mon. Weather Rev., 132, 103–120, 2004.

Hiederer, R. and Köchy, M.: Global soil organic carbon estimates and the harmonized world soil database, EUR, 79, 25225, doi:10.2788/13267, 2011.

Huffman, G. J., Bolvin, D. T., Nelkin, E. J., Wolff, D. B., Adler, R. F., Gu, G., Hong, Y., Bowman, K. P., and Stocker, E. F.: The TRMM Multisatellite Precipitation Analysis (TMPA): Quasi-global, multiyear, combined-sensor precipitation estimates at fine scales, J. Hydrometeorol., 8, 38–55, doi:10.1175/JHM560.1, 2007.

Huntzinger, D. N., Post, W. M., Wei, Y., Michalak, A. M., West, T. O., Jacobson, A. R., Baker, I. T., Chen, J. M., Davis, K. J., Hayes, D. J., Hoffman, F. M., Jain, A. K., Liu, S., McGuire, A. D., Neilson, R. P., Potter, C., Poulter, B., Price, D., Raczka, B. M., Tian, H. Q., Thornton, P., Tomelleri, E., Viovy, N., Xiao, J., Yuan, W., Zeng, N., Zhao, M., and Cook, R.: North American Carbon Project (NACP) Regional Interim Synthesis: Terrestrial Biospheric Model Intercomparison, Ecol. Model., 224, 144–157, doi:10.1016/j.ecolmodel.2012.02.004, 2012.

Joiner, J., Guanter, L., Lindstrot, R., Voigt, M., Vasilkov, A. P., Middleton, E. M., Huemmrich, K. F., Yoshida, Y., and Frankenberg, C.: Global monitoring of terrestrial chlorophyll fluorescence from moderate-spectral-resolution near-infrared satellite measurements: methodology, simulations, and application to GOME-2, Atmos. Meas. Tech., 6, 2803–2823, doi:10.5194/amt-6-2803-2013, 2013.

Jung, M., Reichstein, M., and Bondeau, A.: Towards global empirical upscaling of FLUXNET eddy covariance observations: validation of a model tree ensemble approach using a biosphere model, Biogeosciences, 6, 2001–2013, doi:10.5194/bg-6-2001-2009, 2009.

Laanbroek, H. J.: Methane emission from natural wetlands: interplay between emergent macrophytes and soil microbial processes, A mini-review, Ann. Bot.-London, 105, 141–153, 2010.

Kain, J. S.: The Kain–Fritsch Convective Parameterization: An Update, J. Appl. Meteorol., 43, 170–181, doi:10.1175/1520-0450(2004)043<0170:TKCPAU>2.0.CO;2, 2004.

King, A. W., Andres, R. J., Davis, K. J., Hafer, M., Hayes, D. J., Huntzinger, D. N., de Jong, B., Kurz, W. A., McGuire, A. D., Vargas, R., Wei, Y., West, T. O., and Woodall, C. W.: North America's net terrestrial $CO_2$ exchange with the atmosphere 1990–2009, Biogeosciences, 12, 399–414, doi:10.5194/bg-12-399-2015, 2015.

Kirschke, S., Bousquet, P., Ciais, P., Saunois, M., Canadell, J. G., Dlugokencky, E. J., Bergamaschi, P., Bergmann, D., Blake, D. R., Bruhwiler, L., Cameron-Smith, P., Castaldi, S., Chevallier, F., Feng, L., Fraser, A., Heimann, M., Hodson, E. L., Houweling, S., Josse, B., Fraser, P. J., Krummel, P. B., Lamarque, J.-F., Langenfelds, R. L., Le Quéré, C., Naik, V., O'Doherty, S., Palmer, P. I., Pison, I., Plummer, D., Poulter, B., Prinn, R. G., Rigby, M., Ringeval, B., Santini, M., Schmidt, M., Shindell, D. T., Simpson, I. J., Spahni, R., Steele, L. P., Strode, S. A., Sudo, K., Szopa, S., van der Werf, G. R., Voulgarakis, A., van Weele, M., Weiss, R. F., Williams, J. E., and Zeng, G.: Three decades of global methane sources and sinks, Nat. Geosci., 6, 813–823, doi:10.1038/ngeo1955, 2013.

Lauvaux, T. and Davis, K. J.: Planetary boundary layer errors in mesoscale inversions of column-integrated $CO_2$ measurements, J. Geophys. Res.-Atmos., 119, 490–508, doi:10.1002/2013jd020175, 2014.

Lauvaux, T., Schuh, A. E., Uliasz, M., Richardson, S., Miles, N., Andrews, A. E., Sweeney, C., Diaz, L. I., Martins, D., Shepson, P. B., and Davis, K. J.: Constraining the $CO_2$ budget of the corn belt: exploring uncertainties from the assumptions in a mesoscale inverse system, Atmos. Chem. Phys., 12, 337–354, doi:10.5194/acp-12-337-2012, 2012.

Melack, J. M., Hess, L. L., Gastil, M., Forsberg, B. R., Hamilton, S. K., Lima, I. B. T., and Nova, E. M. L. M.: Regionalization of methane emissions in the Amazon basin with microwave remote sensing, Glob. Change Biol., 10, 530–544, 2004.

Melton, J. R., Wania, R., Hodson, E. L., Poulter, B., Ringeval, B., Spahni, R., Bohn, T., Avis, C. A., Beerling, D. J., Chen, G., Eliseev, A. V., Denisov, S. N., Hopcroft, P. O., Lettenmaier, D. P., Riley, W. J., Singarayer, J. S., Subin, Z. M., Tian, H., Zürcher, S., Brovkin, V., van Bodegom, P. M., Kleinen, T., Yu, Z. C., and Kaplan, J. O.: Present state of global wetland extent and

wetland methane modelling: conclusions from a model intercomparison project (WETCHIMP), Biogeosciences, 10, 753–788, doi:10.5194/bg-10-753-2013, 2013.

Mitsch, W., Nahlik, A., Wolski, P., Bernal, B., Zhang, L., and Ramberg, L.: Tropical wetlands: seasonal hydrologic pulsing, carbon sequestration, and methane emissions, Wetlands Ecol. Manage., 18, 573–586, doi:10.1007/s11273-009-9164-4, 2010.

Miyajima, T., Wada, E., Hanba, Y. T., and Vijarnsorn, P.: Anaerobic mineralization of indigenous organic matters and methanogenesis in tropical wetland soils, Geochim. Cosmochim. Ac., 61, 3739–3751, doi:10.1016/S0016-7037(97)00189-0, 1997.

Myhre, G., Shindell, D., Bréon, F.-M., Collins, W., Fuglestvedt, J., Huang, J., Koch, D., Lamarque, J.-F., Lee, D., Mendoza, B., Nakajima, T., Robock, A., Stephens, G., Takemura, T., and Zhang, H.: Anthropogenic and Natural Radiative Forcing, in: Climate Change 2013: The Physical Science Basis. Contribution of Working Group I to the Fifth Assessment Report of the Intergovernmental Panel on Climate Change, edited by: Stocker, T. F., Qin, D., Plattner, G.-K., Tignor, M., Allen, S. K., Boschung, J., Nauels, A., Xia, Y., Bex, V., and Midgley, P. M., Cambridge University Press, Cambridge, United Kingdom and New York, NY, USA, 2013.

Nakanishi, M. and Niino, H.: An improved Mellor-Yamada level-3 model with condensation physics: its design and verification, Bound.-Lay. Meteorol., 112, 1–31, doi:10.1023/B:BOUN.0000020164.04146.98, 2004.

Pan, H.-L. and Mahrt, L.: Interaction between soil hydrology and boundary-layer development, Bound.-Lay. Meteorol., 38, 185–202, doi:10.1007/BF00121563, 1987.

Parker, R., Boesch, H., Cogan, A., Fraser, A., Feng, L., Palmer, P. I., Messerschmidt, J., Deutscher, N., Griffith, D. W. T., Notholt, J., Wennberg, P. O., and Wunch, D.: Methane observations from the greenhouse gases observing satellite: comparison to ground-based TCCON data and model calculations, Geophys. Res. Lett., 38, L15807, doi:10.1029/2011GL047871, 2011.

Peylin, P., Law, R. M., Gurney, K. R., Chevallier, F., Jacobson, A. R., Maki, T., Niwa, Y., Patra, P. K., Peters, W., Rayner, P. J., Rödenbeck, C., van der Laan-Luijkx, I. T., and Zhang, X.: Global atmospheric carbon budget: results from an ensemble of atmospheric $CO_2$ inversions, Biogeosciences, 10, 6699–6720, doi:10.5194/bg-10-6699-2013, 2013.

Pison, I., Ringeval, B., Bousquet, P., Prigent, C., and Papa, F.: Stable atmospheric methane in the 2000s: key-role of emissions from natural wetlands, Atmos. Chem. Phys., 13, 11609–11623, doi:10.5194/acp-13-11609-2013, 2013.

Prigent, C., Papa, F., Aires, F., Jimenez, C., Rossow, W. B., and Matthews, E.: Changes in land surface water dynamics since the 1990s and relation to population pressure, Geophys. Res. Lett., 39, L08403, doi:10.1029/2012GL051276, 2012.

Riley, W. J., Subin, Z. M., Lawrence, D. M., Swenson, S. C., Torn, M. S., Meng, L., Mahowald, N. M., and Hess, P.: Barriers to predicting changes in global terrestrial methane fluxes: analyses using CLM4Me, a methane biogeochemistry model integrated in CESM, Biogeosciences, 8, 1925–1953, doi:10.5194/bg-8-1925-2011, 2011.

Saatchi, S. S., Harris, N. L., Brown, S., Lefsky, M., Mitchard, E. T., Salas, W., Zutta, B. R., Buermann, W., Lewis, S. L., Hagen, S., Petrova, S., White, L., Silman, M., and Morel, A.: Benchmark map of forest carbon stocks in tropical regions across three continents, P. Natl. Acad. Sci. USA, 108, 9899–9904, doi:10.1073/pnas.1019576108, 2011.

Schimel, D., Stephens, B. B., and Fisher, J. B.: Effect of increasing $CO_2$ on the terrestrial carbon cycle, P. Natl. Acad. Sci. USA, 112, 436–441, doi:10.1073/pnas.1407302112, 2015a.

Schimel, D., Pavlick, R., Fisher, J. B., Asner, G. P., Saatchi, S., Townsend, P., Miller, C., Frankenberg, C., Hibbard, K., and Cox, P.: Observing terrestrial ecosystems and the carbon cycle from space, Glob. Change Biol., 21, 1762–1776, doi:10.1111/gcb.12822, 2015b.

Schroeder, R., McDonald, K. C., Chapman, B. D., Jensen, K., Podest, E., Tessler, Z. D., Bohn, T. J., and Zimmermann, R.: Development and Evaluation of a Multi-Year Fractional Surface Water Data Set Derived from Active/Passive Microwave Remote Sensing Data, Remote Sens., 7, 16688–16732, doi:10.3390/rs71215843, 2015.

Skamarock, W. C. and Klemp, J. B.: A time-split nonhydrostatic atmospheric model for weather research and forecasting applications, J. Comput. Phys., 227, 3465–3485, doi:10.1016/j.jcp.2007.01.037, 2008.

Sweeney, C., Karion, A., Wolter, S., Newberger, T., Guenther, D., Higgs, J. A., Andrews, A. E., Lang, P. M., Neff, D., Dlugokencky, E., Miller, J. B., Montzka, S. A., Miller, B. R., Masarie, K. A., Biraud, S. C., Novelli, P. C., Crotwell, M., Crotwell, A. M., Thoning, K., and Tans, P. P.: Seasonal climatology of $CO_2$ across North America from aircraft measurements in the NOAA/ESRL Global Greenhouse Gas Reference Network, J. Geophys. Res.-Atmos., 120, 5155–5190, doi:10.1002/2014JD022591, 2015.

Turner, A. J., Jacob, D. J., Wecht, K. J., Maasakkers, J. D., Lundgren, E., Andrews, A. E., Biraud, S. C., Boesch, H., Bowman, K. W., Deutscher, N. M., Dubey, M. K., Griffith, D. W. T., Hase, F., Kuze, A., Notholt, J., Ohyama, H., Parker, R., Payne, V. H., Sussmann, R., Sweeney, C., Velazco, V. A., Warneke, T., Wennberg, P. O., and Wunch, D.: Estimating global and North American methane emissions with high spatial resolution using GOSAT satellite data, Atmos. Chem. Phys., 15, 7049–7069, doi:10.5194/acp-15-7049-2015, 2015.

Uliasz, M.: Lagrangian particle modeling in mesoscale applications, Environmental Modelling II, edited by: Zanetti, P., Computational Mechanics Publications, 71–102, 1994.

Veefkind, J. P., Aben, I., McMullan, K., Förster, H., de Vries, J., Otter, G., Claas, J., Eskes, H. J., de Haan, J. F., Kleipool, Q., van Weele, M., Hasekamp, O., Hoogeven, R., Landgraf, J., Snel, R., Tol, P., Ingmann, P., Voors, R., Kruizinga, B., Vink, R., Visser, H., and Levelt, P. F.: TROPOMI on the ESA Sentinel-5 Precursor: A GMES mission for global observations of the atmospheric composition for climate, air quality and ozone layer applications, Remote Sens. Environ., 120, 70–83, doi:10.1016/j.rse.2011.09.027, 2012.

Vukicevic, T., Braswell, B. H., and Schimel, D.: A diagnostic study of temperature controls on global terrestrial carbon exchange, Tellus B, 53, 150–170, doi:10.1034/j.1600-0889.2001.d01-13.x, 2001.

Wecht, K. J., Jacob, D. J., Sulprizio, M. P., Santoni, G. W., Wofsy, S. C., Parker, R., Bösch, H., and Worden, J.: Spatially resolving methane emissions in California: constraints from the CalNex aircraft campaign and from present (GOSAT, TES) and future (TROPOMI, geostationary) satellite observations, Atmos. Chem. Phys., 14, 8173–8184, doi:10.5194/acp-14-8173-2014, 2014.

Whalen, S. C.: Biogeochemistry of methane exchange between natural wetlands and the atmosphere, Environ. Eng. Sci., 22, 73–94, doi:10.1089/ees.2005.22.73, 2005.

Wania, R., Ross, I., and Prentice, I. C.: Implementation and evaluation of a new methane model within a dynamic global vegetation model: LPJ-WHyMe v1.3.1, Geosci. Model Dev., 3, 565–584, doi:10.5194/gmd-3-565-2010, 2010.

Wilson, C., Gloor, M., Gatti, L. V., Miller, J. B., Monks, S. A., McNorton, J., Bloom, A. A., Basso, L. S., and Chipperfield, M. P.: Contribution of regional sources to atmospheric methane over the Amazon Basin in 2010 and 2011, Global Biogeochem. Cy., 30, 400–420, doi:10.1002/2015GB005300, 2016.

Worden, J., Kulawik, S., Frankenberg, C., Payne, V., Bowman, K., Cady-Peirara, K., Wecht, K., Lee, J.-E., and Noone, D.: Profiles of $CH_4$, HDO, $H_2O$, and $N_2O$ with improved lower tropospheric vertical resolution from Aura TES radiances, Atmos. Meas. Tech., 5, 397–411, doi:10.5194/amt-5-397-2012, 2012.

Worden, J., Doran, G., Kulawik, S., Eldering, A., Crisp, D., Frankenberg, C., O'Dell, C., and Bowman, K.: Evaluation And Attribution Of OCO-2 $XCO_2$ Uncertainties, Atmos. Meas. Tech. Discuss., doi:10.5194/amt-2016-175, in review, 2016.

Yokota, T., Yoshida, Y., Eguchi, N., Ota, Y., Tanaka, T., Watanabe, H., and Maksyutov, S.: Global concentrations of $CO_2$ and $CH_4$ retrieved from GOSAT: First preliminary results, SOLA, 5, 160–163, doi:10.2151/sola.2009-041, 2009.